Covalently-bonded single-site Ru-N$_2$ knitted into covalent triazine frameworks for boosting photocatalytic CO$_2$ reduction

Lu Wang [a,1], Lin Wang [a,*,1], Saifei Yuan [a], Liping Song [a], Hao Ren [a], Yuankang Xu [a], Manman He [a], Yuheng Zhang [a], Hang Wang [a], Yichao Huang [a], Tong Wei [a], Jiangwei Zhang [b,*], Yuichiro Himeda [c,*], Zhuangjun Fan [a,*]

[a] School of Materials Science and Engineering, China University of Petroleum (East China), Qingdao 266580, China
[b] College of Chemistry and Chemical Engineering, Inner Mongolia University, Hohhot 010021, China
[c] Global Zero Emission Research Center, National Institute of Advanced Industrial Science and Technology, Tsukuba, Ibaraki 305-8569, Japan

ARTICLE INFO

ABSTRACT

Harvesting solar energy to convert CO$_2$ into chemicals via photocatalysis has received increasing attention, however, lack of precisely controlled and uniformly dispersed active sites usually leads to low selectivity and activity. Herein, we present an *in situ* covalent-bonding strategy for the first time to knit well-defined single-site Ru-N$_2$ into conjugated covalent triazine frameworks (CTFs) for highly selective photoreduction of CO$_2$. The resulting Ru-CTF enhanced charge separation and stabilized the molecular catalyst, providing a solar-to-formate conversion rate of 2090 μmol·g$_{cat}^{-1}$·h^{-1} with a selectivity of 98.5 % without extra photosensitizer, which greatly outperforms most other reported photocatalysts. Experiments and DFT calculations demonstrate that the single-site Ru-N$_2$ could easily activate CO$_2$ and the H$_2$O-substituted Ru-N$_2$ unit is the newly discovered active center for the efficient photocatalysis. This work paves a new way and significant understandings to design single-site CTF-based photocatalysts for highly selective CO$_2$ photoreduction.

1. Introduction

The solar-light-driven CO$_2$ reduction reaction (CO$_2$RR) is expected to perfectly mimic natural photosynthesis, enabling the sustainable production of high-value-added chemicals or fuels in a more environmentally friendly manner [1,2]. Among the CO$_2$ conversion strategies, the selective reduction of CO$_2$ to liquid formate via photocatalysis possesses broad application prospects [3–15]. It is a promising liquid organic hydrogen carrier that can store and release H$_2$ in the presence of suitable catalysts [16,17]. The reduction/re-oxidation process thus can complete a carbon-neutral cycle without release of harmful byproducts [18]. This strategy can create renewable energy fuels and chemical raw materials, which has important scientific research values in the field of energy storage and transformation.

To attain high CO$_2$RR activity and selectivity, various semiconductor catalysts, such as Ta$_2$O$_5$ [19], TiO2 [20], and *g*-C$_3$N$_4$ [21,22], have been implemented. However, these traditional semiconductor-based photocatalysts are usually difficult to atomic-scale regulate and control the

photoelectrochemical performances, hampering the improvements on the photocatalytic performance. Recently, porous organic materials, including covalent organic frameworks (COFs) [14,15,23–26], metal organic frameworks (MOFs) [3–9,27,28] and conjugated microporous polymers (CMPs) [10,29,30], have shown great potential in photocatalysis CO$_2$RR owing to their well-defined and tailorable structures. However, to our knowledge, CO$_2$RR using covalent triazine frameworks (CTFs) as a photocatalyst remain extremely rare [31]. Since pioneered by Thomas [32], covalent triazine frameworks (CTFs) have emerged as interesting platforms in the field of CO$_2$ capture and storage, photocatalysis and energy storage due to their π-conjugated nitrogen-rich structures, molecularly precise backbones and tunable chemical structures, which provide a broad molecular-level platform for designing efficient polymer materials [33–36]. At present, numerous CTFs have been designed and studied in photocatalytic hydrogen evolution [33,34, 37], but research on photocatalytic CO$_2$RR is rarely due to lack of precisely controlled and uniformly dispersed active sites. In recent years, single-atom catalysts have attracted considerable interest owing to

---

maximum atom-utilization efficiency, fast charge transfer and targeting active sites for the enhancement of photocatalytic activities [23,38,39]. CTFs as the versatile platforms can effectively integrate a single-site molecular catalysts via selection of appropriate bridging ligands with triazine units as connecting nodes, thereby enabling efficient photosensitization of multielectron reduction catalysis. For example, the ligand of 2,2′-bipyridine-5,5′-dicarbonitrile (dcbpy) is an ideal linker for constructing functionalized CTFs photocatalysts for photocatalytic CO_2 reduction due to the strong coordination ability of bipyridine unit [28, 40].

Ruthenium(II)-based photocatalytic molecular catalysts were considered to be high-selective active sites to produce formate under visible light [18,21,22]. However, it is difficult to isolate the products and recycle the catalysts for homogeneous catalytic systems [41,42]. The knitting of a molecular catalyst into the photo-responsive porous materials can not only enhance the photocatalytic performances by stabilizing the molecular catalyst and promoting electron transfer between photosensitive and catalytic units, but also facilitate the photocatalysis without any additional costly photosensitizers [28].

Herein, we report a newly devised photocatalyst via a new strategy for the first time by knitting the precise single site (H_2O-substituted Ru-N_2) into the photo-responsive CTFs for highly selective photoreduction of CO_2 to formate. Firstly, the strategy of post-modification of Ru sites into a preformed framework (dcbpy-CTF, Fig. 1A) was unsuccessful, because the preformed frame dcbpy-CTF could not be synthesized by the superacid method due to the formation of a salt by the reaction of pyridine moieties with trifluoromethanesulfonic acid (Fig. 1 and Fig. S6) [43]. Significantly, employing metal-coordinated molecules as building blocks was successfully applied to in-situ construct the single-site photocatalysts (Ru-CTFs, Fig. 1B). Therefore, the molecular catalysts direct knitted CTFs with robust covalently-bonded interfacial contact and high charge transfer efficiency can be constructed, which would benefit the spatial separation of photogenerated carriers. In addition, this effectively knitted strategy can prevent the dimerization of the molecular active sites and its deactivation, thus leading to better photocatalytic performance and recyclability. The resulting Ru-CTF provides a solar-to-formate conversion rate of 2090 $\mu mol \cdot g_{cat}^{-1} \cdot h^{-1}$ with a selectivity of 98.5 % without any additional costly photosensitizers, which greatly outperforms most other reported photocatalysts. Experiments and DFT calculations demonstrate that the single-site Ru-N_2 could easily activate

CO_2 and the H_2O-substituted Ru unit is more favorable to form the key intermediate metal hydride to react with CO_2 with a much lower free energy barrier than that of dicarbonyl Ru unit, thus realizing high catalytic activity and selectivity for CO_2RR.

2. Experimental section

2.1. Materials

All chemicals, unless otherwise stated, were purchased from commercial sources. *N,N*-dimethylacetamide (DMA) and triethanolamine (TEOA) were dried over 4 Å molecular sieves and kept under Ar prior to use. [Ru(dcbpy)(CO)$_2$Cl$_2$] were synthesized based on previously reported methods (see the details in Supporting information) [44,45].

2.2. Synthesis of Ru-CTFs

Covalent triazine frameworks (CTFs) were prepared by using trifluoromethanesulfonic acid (CF_3SO_3H) as the catalyst [33,37]. [Ru (dcbpy)(CO)$_2$Cl$_2$] (0.0108 g, 0.025 mmol) and 4,4′-biphenyldicarbonitrile (0.1174 g, 0.575 mmol) were added into a pre-dried flask, then 3.24 g (21.6 mmol) of CF_3SO_3H was added under nitrogen at 0 °C. The obtained orange red solution was then stirred for 0.5 h to completely dissolve the monomers before the heating treatment of 120 °C for 10 min. The solution was then warmed at 100 °C and kept stirring at this temperature for 2 h to initiate the trimerization reaction of terminal cyano groups and form the Ru-CTF oligomer. Then the solution was further stirred at 80 °C for 10 h to allow complete conversion to the polymer. The obtained deep red solution was then quenched by ethanol for obtaining the precipitated golden solid (Fig. S3). After that, the mixture was poured into diluted ammonia solution and stirred for 12 h. Notably, the suspension changed color from golden yellow to red-brown (Fig. S3). The precipitates were filtered and further purified by Soxlet extraction with ethanol, methanol and dichloromethane, respectively. Finally, the obtained red-brown solid was grounded into powder with an agate mortar (63 % yield). Ru-CTFs with various loading amounts of Ru (dcbpy)(CO)$_2$Cl$_2$ were denoted as Ru-CTF-3, Ru-CTF-2, Ru-CTF-1. The dcbph-CTF was prepared by the same method without addition of Ru (dcbpy)(CO)$_2$Cl$_2$. ICP-AES analysis of the digested samples revealed that the Ru contents in Ru-CTF-1, Ru-CTF-2, and Ru-CTF-3 were nearly 0.68,
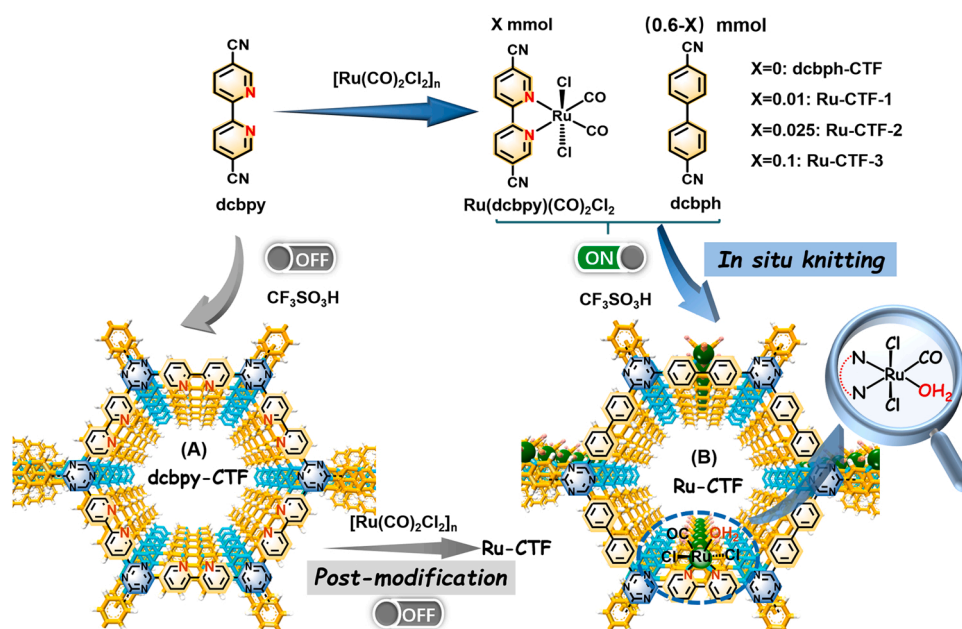

Fig. 1. Schematic representation of the *in situ* knitting strategy for Ru-CTFs.

1.76 and 5.96 wt%, respectively.

2.3. General characterizations

Scanning electron microscopy (SEM) images were obtained using a Hitachi SU8010 microscope. Energy-dispersive X-ray spectroscopy (EDX) mapping images were obtained using a TESCAN MIRA3 FEG-SEM instrument. Raman spectra were measured on a Raman spectrometer Labram HR evolution (Horiba JobinYvon, France). X-ray photoelectron spectra (XPS) were obtained using a Thermo scientific XPS K-alpha 250Xi surface analysis machine using an Al source. Analysis was performed using XPS Peak 4.1 software. All binding energies were calibrated to the C 1 s peak at 284.6 eV. N_2 adsorption isotherms were collected on a Quantachrome Instruments Autosorb-iQ (Boynton Beach, Florida USA) at 77 K from 0 to 1 atm. The samples were activated before adsorption measurements. UV-Vis diffused reflectance spectra (DRS) were obtained using a spectrometer (UV-2700, Shimadzu, Japan) by measuring the reflectance of powders in the solid state. Powder X-ray diffraction (PXRD) patterns were obtained with a Bruker D8 diffractometer (German) equipped with Cu/Kα radiation (λ = 1.5418 Å). Metal content analysis was obtained by inductively coupled plasma-atomic emission spectrometry (ICP-AES) using the iCAP 7400 spectrometer (Thermo Fisher Scientific, USA). ^1H and ^{13}C NMR spectra were obtained in solution using a Bruker Advance 400 NMR spectrometer. Fourier-transform infrared spectra (FTIR) were collected by Shimadzu IRTracer-100 FT-IR spectrometer in attenuated total reflection (ATR) infrared mode. The samples were compressed on a ZnSe window. The photoluminescence (PL) spectra were recorded with an Edinburgh Instruments FL920 spectrofluorometer (λ_{ex} = 375 nm).

2.4. In situ attenuated total reflection-infrared (ATR-IR)

The *in situ* attenuated total reflection-infrared (ATR-IR) spectra were performed on Shimadzu IRTracer-100 equipped with a single reflection silicon ATR module and IR cell (Fig. S4) with IR incidence at 45 degrees. Firstly, the sample was treated under dynamic vacuum at 80 °C for 2 h. Then the solution with a catalyst was purged with CO_2 (99.999 %), after reaching adsorption equilibrium, an ATR-IR spectrum was collected. The solutions for photocatalytic CO_2 conversion were irradiated by a 300 W Xe-lamp (FX300, Beijing Perfect Light Technology Co., Ltd., Beijing, China). And in order to prevent evaporation of solvent and provide good light transmission, liquid samples kept covered with quartz. The ATR-IR spectra were recorded every 2 min at the resolution of 8 cm^{-1} and 150 scans.

2.5. X-ray absorption measurements (XAFS) and analysis

The Ru K-edge XAFS were obtained at BL14W1 beamline of Shanghai Synchrotron Radiation Facility (SSRF), China. The data of Ru K-edge were obtained in transmission mode by using a Lytle detector. The acquired XAFS data were then processed by background-subtracted and normalized with the ATHENA module of Demeter software packages. Subsequently, the quantitative curve fittings of the EXAFS χ(k) data was carried out with the ARTEMIS module of Demeter software packages.

2.6. Photoelectrochemical measurements

All photoelectrochemical measurements were measured in 0.2 M Na_2SO_4 solution via a CHI 660E electrochemical station (Shanghai Chenhua Co.) in a standard three electrode configuration. The details are as below: 10 mg catalysts were dispersed in 0.2 mL ethanol containing 20 μL 5 wt% Nafion D-520, and then sonicated 10 min to generate a homogeneous slurry. Subsequently, 60 μL slurry was coated on the indium tin oxides (ITO) conductive glass substrate with the area 1×1 cm^{-2} as working electrode, and then dried at 60 ºC in vacuum oven for 12 h.

2.7. Photocatalytic measurement of CO_2 reduction

The photocatalytic CO_2 reduction experiments were carried out in Parallel Light Reactor (WP-TEC-1020HSL, WATTCAS, China) (Fig. S5). 0.5 mg of catalyst, 0.75 mL of DMA, and 0.25 mL of TEOA were dispersed in a 20 mL quartz tube. Then the vessel was sealed with a rubber stopper. The mixture was purged with CO_2 (99.999 %) by evacuated and backfilled CO_2 three times. Next, the reaction mixture was vigorously stirred and a LED lamp (8 W) was served as the visible light source by bottom-irradiation. The reaction system was kept at 20 °C with a circulating cooling water system during irradiation. The amount of formate product was measured by high-performance liquid chromatography (HPLC) system (LC-2030 Plus, Shimadzu. Japan) at a wavelength of 210 nm with 20 mM H_3PO_4 as the mobile phase. Gaseous products were detected by gas chromatography (GC-2014, Shimadzu. Japan).

2.8. The density functional theory (DFT) calculations

The catalytic reaction mechanism was assessed by DFT calculations with constraint models, where the electron-electron interactions were described with the hybrid B3LYPM06 functional implemented in the Gaussian 16 package. The moderate size basis set 6-31 G* was used in structure optimization and frequency analysis, while the energetics and electronic structures were calculated with a much larger basis set 6-311 + +G basis set on the optimized structures. The LANL08 relativistic effective core potential and basis set were used for the Ru atoms. In all the calculations, the self-consistent reaction field method with the polarizable continuum model (SCRF-PCM) was used to implicitly account for the solvent effects.

3. Results and discussion

3.1. Synthesis and structural analysis of single-site Ru-N$_2$ photocatalyst

According to the synthetic approach in Fig. 1, Ru(dcbpy)(CO)$_2$Cl$_2$ was first prepared with [Ru(CO)$_2$Cl$_2$]$_n$ and dcbpy, then Ru-CTFs with different molar amounts of Ru(dcbpy)(CO)$_2$Cl$_2$ (X = 0, 0.01, 0.025, 0.1) and dcbph precursor (0.6-X) were fabricated and named as dcbph-CTF, Ru-CTF-1, Ru-CTF-2, and Ru-CTF-3, respectively. The structures of the synthesized CTFs were first confirmed by using the Fourier transform infrared (FT-IR) technique (Fig. 2a). The successful formation of triazine structures in these CTFs were confirmed by the C=N stretching bands (1566, 1500 and 801 cm^{-1}) and C-N stretching vibration band (1356 cm^{-1}) in the FT-IR spectra (Fig. 2a) [33,46]. Compared to dcbph-CTF, an additional peak at 1960 cm^{-1} was observed in the spectra of Ru-CTF, attributing to the stretching vibration of v(C=O) in the Ru(dcbpy)(CO)$_2$Cl$_2$ moiety [20]. Notably, with the increase of Ru content in CTFs, the intensity of peak at 1960 cm^{-1} obviously increased (Fig. 2b). In addition, compared with those of the precursor Ru(dcbpy)(CO)$_2$Cl$_2$ (2072 and 2011 cm^{-1}), Ru-CTF-2 exhibited the v(C=O) stretching vibration (1960 cm^{-1}) with a red shift due to the dissociation of one CO, which would lead to the formation of the pentacoordinated intermediate and thus favoring the rapid formation of the important CO_2 adduct in the photocatalytic process [20,45,47].

As compared with dcbph-CTF, the additional peaks in the high-resolution C 1 s + Ru 3d X-ray photoelectron spectroscopy (XPS) spectrum of Ru-CTF-2 (Fig. 2c) at about 281.5 eV and 285.6 eV corresponded to Ru^{II} 3d$_{5/2}$ and 3d$_{3/2}$ states, respectively [48]. Moreover, these values corresponded well with those of the precursor Ru(dcbpy)(CO)$_2$Cl$_2$, indicating that the Ru-N$_2$ active sites were successfully knitted in the CTFs. Meanwhile, the C1s binding energy (Fig. 2c) at 286.6 eV and the N 1 s binding energy (Fig. S7) at 398.4 eV also confirmed the formation of triazine structure [37,46]. Additionally, the elemental mapping analysis by energy-dispersive X-ray spectroscopy (EDX) (Fig. S8) and inductively coupled plasma-atomic emission spectrometry
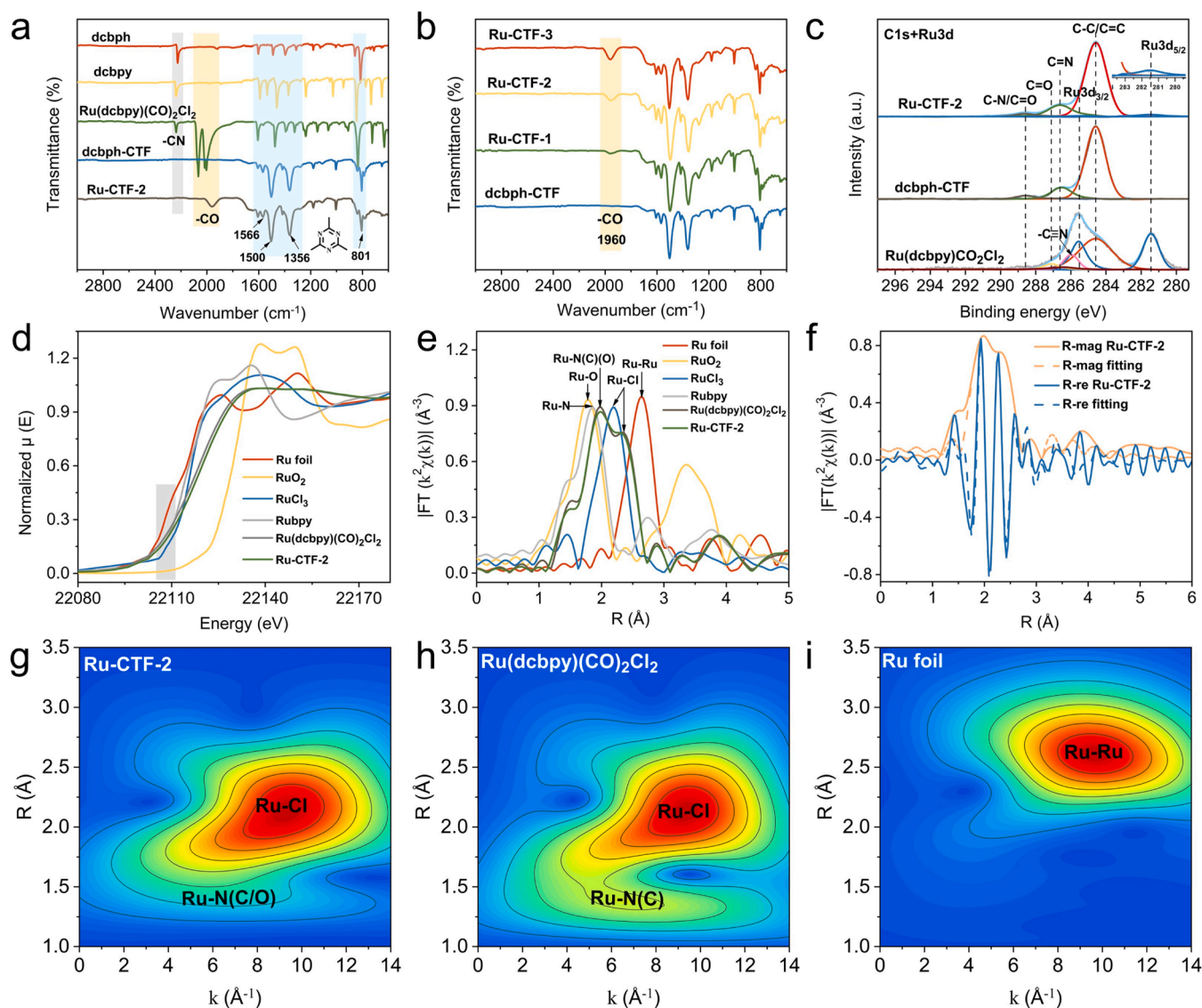
Fig. 2. FT-IR spectra of (a) CTFs and precursor and (b) CTFs with different Ru content. (c) C 1 s + Ru 3d XPS spectra of Ru-CTF-2, dcbph-CTF and Ru(dcbpy)(CO)$_2$Cl$_2$, respectively. (d) Normalized Ru K-edge XANES spectra and (e) corresponding k2-weighted Fourier transform spectra from Ru K-edge EXAFS of Ru foil, RuO$_2$, RuCl$_3$, Rubpy, Ru(dcbpy)(CO)$_2$Cl$_2$ and Ru-CTF-2. (f) χ(R) space spectra fitting curve of EXAFS spectra of Ru-CTF-2. Ru K-edge wavelet transform (WT)-EXAFS for (g) Ru-CTF-2, (h) Ru(dcbpy)(CO)$_2$Cl$_2$ and (i) Ru foil.

(ICP-AES) demonstrated the presence of Ru elements in Ru-CTF-2. The synthesized Ru-CTF-2 exhibited irregularly stacked chunks and compact layer structure as observed from the scanning electron microscopy (SEM) images (Fig. S8). The Powder X-ray diffraction (PXRD) patterns of CTFs exhibited the limited crystallinity (Fig. S9) [37,46]. Based on the N$_2$ adsorption-desorption isotherms (Fig. S10), all the CTFs showed low specific surface areas, which could be attributed to the stacking of the amorphous CTF, consistent with previous CTFs studies [46,49,50].

To probe the coordination environment of the Ru atoms in the Ru-CTF photocatalyst, the Ru K-edge X-ray absorption near-edge structure (XANES) and extended X-ray absorption fine structure (EXAFS) data were obtained for Ru-CTF-2, Ru(dcbpy)(CO)$_2$Cl$_2$ precursor and related reference materials. As shown in the Ru K-edge XANES spectra (Fig. 2d), Ru-CTF-2 gave nearly the same signals as the Ru(dcbpy)(CO)$_2$Cl$_2$ precursor, the energy absorption threshold values of them were between Ru foil and RuCl$_3$, and overlapping the position of tris(2,2′-bipyridyl) dichlororuthenium(II) hexahydrate (Rubpy), implying that the stable valence state of Ru in Ru-CTF-2 was close to 2, which was consistent with the analysis of XPS.

In addition, the k2-weighted Fourier transformed EXAFS (FT-EXAFS) for the Ru K-edge (Fig. 2e) of Ru-CTF-2 was well fit with Ru(dcbpy)(CO)$_2$Cl$_2$ sample, affording nearly identical coordination geometry and bond lengths. As a result, the peak at 1.97 Å was corresponding to the Ru-N(C)(O) coordination environment and the shoulder peak located at 2.36 Å was attribute to scattering path of Ru-Cl bonds for Ru-CTF-2 and Ru(dcbpy)(CO)$_2$Cl$_2$. Notably, in contrast to the Ru foil, Ru-CTF-2 did not show a prominent peak at 2.64 Å for the Ru-Ru bond, supporting the conclusion that the atomically dispersed Ru atoms were anchored on the CTF framework. Additionally, the above result was further intuitively verified by wavelet transform (WT) analysis of the Ru K-edge EXAFS oscillation (Fig. 2g-i and Fig. S11).

Moreover, the EXAFS fitting curve (Fig. 2f, Fig. S11 and Table S1) in k space and R space for Ru-CTF-2 and Ru(dcbpy)(CO)$_2$Cl$_2$ samples suggested that the coordination number (CN) of the central atom Ru was six. By comparing the scattering path intensity (Table S1) of Ru-N(C)(Cl)(O) bonds in Ru-CTF-2 and Ru(dcbpy)(CO)$_2$Cl$_2$, the Ru-C coordination number in Ru-CTF-2 was lower than that in Ru(dcbpy)(CO)$_2$Cl$_2$. Significantly, Ru-CTF-2 displayed Ru-C bonding at 1.93 Å with

coordination numbers close to 1, Ru-O bonding at 2.10 Å with coordination numbers close to 1, thus clearly indicating that one CO detached from Ru atoms in Ru-CTF-2 with one coordinated H_2O molecule coordination, which was also consistent with the result of FT-IR characterization. Thus, all the above-mentioned results indicated that H_2O-substituted Ru-N_2 single-sites were successfully *in situ* knitted into the covalent triazine frameworks.

3.2. Photocatalytic performances for CO₂RR

The photocatalytic CO_2 reduction was carried out under visible light irradiation (Fig. S12). Formate as the liquid product was detected and quantified by the HPLC technology and ^1H NMR spectroscopy (Figs. S13 and S14), and the gaseous products were detected and quantified by gas chromatography (GC) (Fig. S15). Among these catalysts, Ru-CTF-2 reached the highest rate of 2090 μmol·g_{cat}^{-1}·h^{-1} in 3 h (Fig. S16), which was higher than that of most reported photocatalysts without extra photosensitizer so far (Fig. 3c and Table S4). As shown in Fig. 3a, under continuous visible light illumination, formate was generated

immediately and exhibited a time-dependent increase with Ru-CTF-2 as the photocatalyst. In contrast, the precursor Ru(dcbpy)(CO)$_2$Cl$_2$ or physically mixed dcbph-CTF with Ru(dcbpy)(CO)$_2$Cl$_2$ showed a much lower activity than that of the knitted single-site heterogeneous system and deactivated rapidly within 1 h, possibly due to the dimerization or decomposition as previously reported [28,51]. Noteworthily, the high selectivity for photocatalytic CO_2 to formate was obtained by Ru-CTF-2 (98.5 %, Fig. 3b). In this work, using DMA/TEOA system for photocatalytic CO_2RR with Ru-CTF-2, HCOO$^-$ is the only photocatalytic liquid product detected by HPLC, whereas traces of gaseous CO and CH_4 byproducts are tested by GC, no subsidiary H_2 was produced throughout the reaction. In addition, we have performed a series of control experiments with different solvent systems and sacrificial electron donors using Ru-CTF-2 as the photocatalyst (Fig. S17 and S18), confirming that the photocatalytic activity and selectivity of Ru-CTF-2 in the CO_2RR depended strongly on the solvent and sacrificial electron donor employed. In addition, rapid deactivation of the homogeneous system was further supported by UV-Vis absorption spectra, in which obvious changes of Ru(dcbpy)(CO)$_2$Cl$_2$ (Fig. 3d) was observed upon light
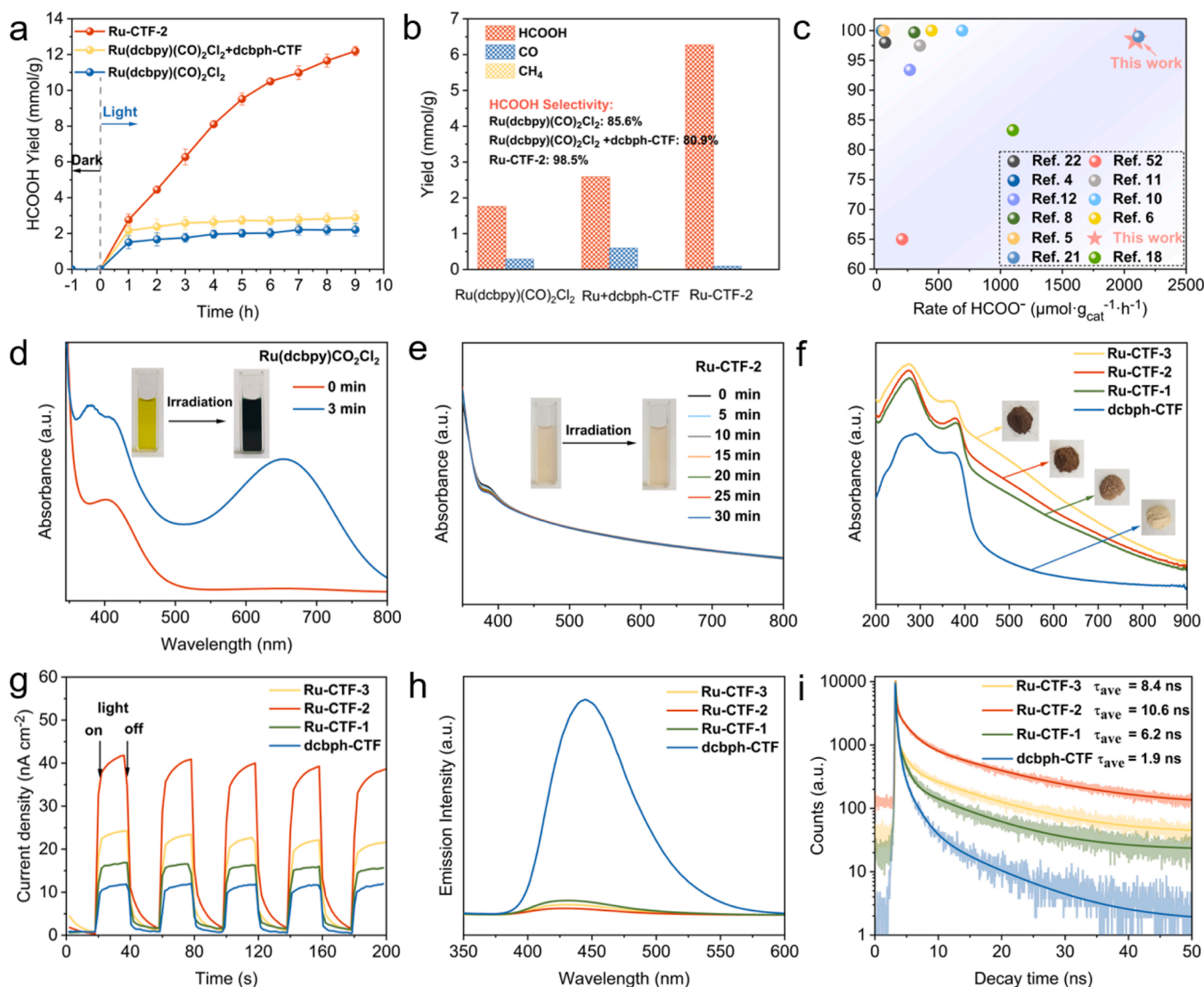
Fig. 3. (a) Amount of formate generated from CO_2 as a function of the irradiation time over heterogeneous Ru-CTF-2, homogeneous Ru(dcbpy)(CO)$_2$Cl$_2$, and physically mixed Ru(dcbpy)(CO)$_2$Cl$_2$ with dcbph-CTF. (b) The selectivity of HCOO$^-$ and the yield distribution of different photoreduction products in 3 h. (c) Comparison of formate selectivity and activity of reported photocatalysts without extra photosensitizer under visible light irradiation. UV-Vis absorption changes for (d) homogeneous Ru(dcbpy)(CO)$_2$Cl$_2$ and (e) heterogeneous Ru-CTF-2 in DMA at different irradiation times. (f) UV/Vis DRS, (g) Transient photocurrent responses, (h) steady-state PL and (i) Time-resolved PL spectra of all samples.

irradiation, while covalently-bonded heterogeneous Ru-CTF-2 (Fig. 3e) showed almost no change with the extension of light irradiation time. Therefore, the above results indicated that the molecular catalysts direct knitted CTFs with robust covalently-bonded interfacial contact would stabilize the molecular catalyst, resulting in a better photocatalytic performance. To further prove the photocatalytic durability, Ru-CTF-2 was recycled and reused at least three runs without a significant decrease in activity (Fig. S19). Moreover, corresponding SEM images, Raman and FTIR spectra of Ru-CTF-2 after the cycling test were also recorded (Fig. S20), no substantial changes could be observed after three cycles, confirming its favorable photocatalytic stability. Moreover, only minimal 0.02 % metal leaching to the solution after recycling could be detected, further revealing the stability of Ru-CTF-2 in photocatalysis.

Control experiments were conducted to further understand the CO_2 reduction under various conditions. The CO_2 reduction processes in the absence of Ru-CTF-2/visible light/CO_2 were performed, affording negligible amount of formate (Fig. S21). Above results suggested that the photocatalyst, light irradiation, and CO_2 were all essential for

formate production in this photocatalytic system. Furthermore, the dependence of formate production on irradiation wavelength indicated that the performance of formate production matched well with the photon absorption properties of Ru-CTF-2 (Fig. S22), further proving that the reaction was indeed induced by light absorption.

3.3. Photoelectrochemical measurements

To understand the excellent photocatalytic activity of Ru-CTF-2, we further characterized the optical properties and the separation of photogenerated carriers. As shown in UV–vis diffuse reflectance spectra (Fig. 3f), the enhanced light absorption was observed after introducing Ru, which was ascribed to the MLCT (metal-to-ligand charge transfer) process of Ru unit at the absorption from 400 to 500 nm (Fig. S23) [52, 53]. In addition, transient photocurrent responses (Fig. 3g) and electrochemical impedance spectroscopy (EIS) (Fig. S24) indicated that Ru-CTF-2 showed the optimal effect on the separation of photogenerated electron-hole pairs. Notably, with the further increase of Ru
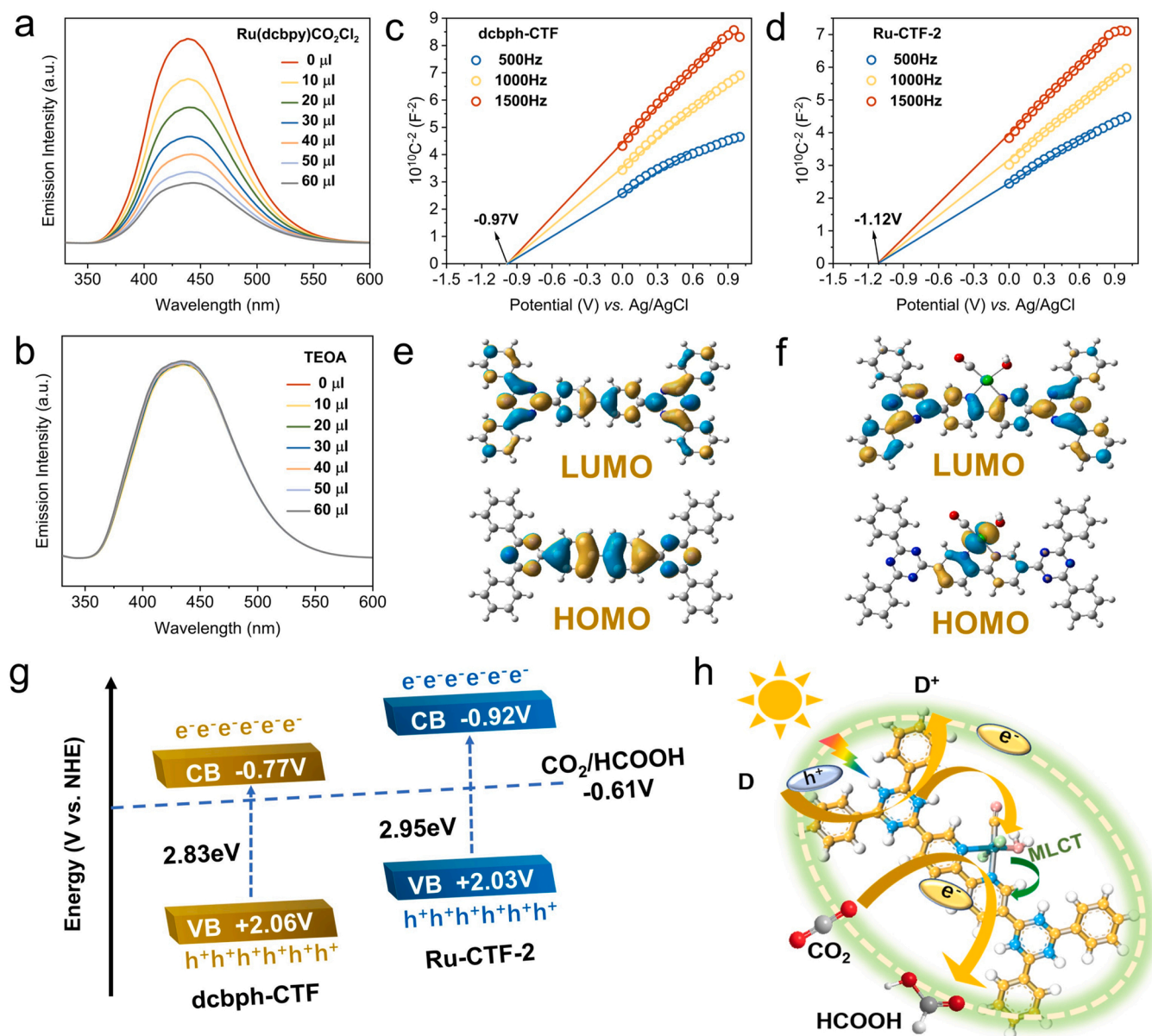
Fig. 4. Photoluminescence spectra of the dcbph-CTF after the addition of different amounts of (a) Ru(dcbpy)(CO)$_2$Cl$_2$ and (b) TEOA in DMA with 320 nm excitation at room temperature. Mott-Schottky plots of (c) dcbph-CTF and (d) Ru-CTF-2. Local density of states (LDOS) plots of (e) dcbph-CTF and (f) Ru-CTF estimated by DFT calculations, respectively. (g) The band diagram of the dcbph-CTF and the Ru-CTF-2 catalysts. (h) The mechanism of photoreduction CO_2 by the Ru-CTF catalyst.

contents, the defects of CTFs may increase, thus causing less efficient electron transfer and separation, which was consistent with the results of photocatalytic performance. The photocurrent hysteresis phenomenon of CTFs sample is generally resulted from a large series resistance during the photocurrent measurement, thus leading to slow rise and fall for the photocurrent curve [54]. The measured steady-state photoluminescence (PL) spectra (Fig. 3h) of Ru-CTF-2 showed a much lower PL intensity than that of dcbph-CTF, suggesting the existence of electron transfer and lower radiative recombination of photogenerated electron-hole pairs after introducing the Ru-N$_2$ site. In addition, fitting of the time-resolved fluorescence (TRPL) spectra (Fig. 3i) revealed that the photogenerated charge carriers survived longer on the surface of Ru-CTF-2. Therefore, these results indicated that the knitted Ru-N$_2$ single-site CTFs would inhibit the fast radiative recombination of photogenerated electron-hole pairs and promote electron transfer between CTF support and Ru-N$_2$ active centers, thus resulting in a better photocatalytic performance.

3.4. Photocatalytic mechanisms and density functional theory (DFT) calculations

To further understand the role of the single-site Ru-N$_2$ unit in the photocatalytic CO$_2$RR, photoluminescence measurement of the catalytic system was performed first. The luminescence quench experiments of dcbph-CTF were studied with addition of TEOA and Ru(dcbpy)(CO)$_2$Cl$_2$, respectively. As shown in Fig. 4a and b, the luminescence of dcbph-CTF support was efficiently quenched by Ru(dcbpy)(CO)$_2$Cl$_2$ but not by TEOA, indicating that the photocatalytic reduction of CO$_2$ process occurred via electron transfer from the photoexcited CTF support to the Ru-N$_2$ unit, but not from TEOA to the excited CTF support, thus suggesting an oxidative quenching mechanism in this photocatalytic process [8,27,28]. Finally, the oxidized CTF support was reduced by TEOA to complete the redox cycle. Above results indicated that the integration of single-site Ru-N$_2$ unit with CTF support could effectively suppress the recombination of photogenerated electron-hole pairs and promote the electron transfer.

Additionally, to investigate the theoretical feasibility for the photocatalytic conversion of CO$_2$ to formate, the conduction band (CB) positions of catalysts were examined by Mott-Schottky measurements. Accordingly, the CB of dcbph-CTF (Fig. 4c) and Ru-CTF-2 (Fig. 4d) were calculated to be -0.77 and -0.92 V versus the normal hydrogen electrode (NHE). And the valence band (VB) positions of the Ru-CTF-2 and dcbph-CTF were determined to be 2.03 and 2.06 V (vs. NHE) associated with Tauc plot for band-gap calculation of CTFs (Fig. S25). As shown in Fig. 4g, the CB position of the Ru-CTF-2 catalyst was higher than that of E$_0$ (CO$_2$/HCOOH = -0.61 V vs NHE), indicating that CO$_2$ could be thermodynamically accelerated to the formation of formate. In order to further explore the possible charge-transfer pathway in Ru-CTF between Ru-N$_2$ site and dcbph-CTF support, the energy of Ru(dcbpy)(CO)$_2$Cl$_2$ was measured by cyclic voltammetry (CV) in DMA with 0.1 M TBAP as supporting electrolyte [55]. Based on the data of CV, the LUMO value of Ru(dcbpy)(CO)$_2$Cl$_2$ was -1.25 V vs. NHE (Fig. S26a), suggesting a more negative reduction potential than that of CO$_2$/HCOOH (-0.61 V vs. NHE). Furthermore, the energy band gap of Ru(dcbpy)(CO)$_2$Cl$_2$ could be calculated from the luminescence emission peak at 550 nm (Eg = 2.25 eV, Fig. S26b). With a comprehensive consideration of the band structures and the reduction potentials of dcbph-CTF support and Ru(dcbpy)(CO)$_2$Cl$_2$, a possible charge-transfer pathway of a direct Z-scheme molecular heterostructures in Ru-CTF was demonstrated as shown in Fig. S27. Such a direct Z-scheme charge-transfer process significantly contributed to the efficient charge separation in the Ru-CTF.

In addition, we performed systematic DFT calculations to assess the electronic structures and possible reaction pathways in the dcbph-CTF and Ru-CTF systems. Local density of states (LDOS) plots showed that the HOMO and LUMO for dcbph-CTF (Fig. 4e) localized on the diphenyl and triazine units, respectively; while for Ru-CTF (Fig. 4f), the HOMO

was located at the Ru unit, the LUMO was mainly located at the dcbpy ligand, implying that the H$_2$O-substituted Ru-N$_2$ center would be a good metal-to-ligand charge transfer (MLCT) acceptor-donor pair and would be feasible for electron-hole separation. Based on the above results, the photocatalytic CO$_2$ reduction mechanism of the Ru-CTF-2 catalyst was proposed in Fig. 4h. Under visible light irradiation, CTF support could absorb photons of visible light to excite electrons and transfer electrons to the Ru-N$_2$ site, thus reducing the adsorbed CO$_2$ molecule to formate. Finally, the holes in the excited CTF support could be reduced by sacrificial donor (TEOA) to complete the catalytic cycle.

3.5. Reaction mechanisms of CO$_2$ to HCOO⁻ on the single-site Ru-N$_2$

To further investigate the reaction mechanism of producing formate over Ru-CTF in reaction thermodynamics, we simulated the adsorption energy of CO$_2$ over surfaces of dcbph-CTF, dcbpy-CTF and Ru-CTF structural model by first-principles calculations based on DFT at first. The introduction of Ru and N sites (Fig. 5a, b and Fig. S28) could enhance the CO$_2$ absorption capacity of Ru-CTF, and notably, the linear structure of CO$_2$ was also bent, demonstrating that Ru-N$_2$ site could easily activate CO$_2$, which was facilitated to start the whole reaction.

In addition, the *in situ* attenuated total reflection-infrared (ATR-IR) spectroscopy (Fig. 5c) was investigated to probe the reaction intermediates in the photocatalytic reaction. Metal hydrides are considered to be the key intermediates in the conversion of CO$_2$ to formate [56]. As shown in Fig. 5c, the peaks at 2017, 1942, 1891 and 1867 cm^{-1} corresponded to metal hydride Ru-H [56]. Then, the CO$_2$ coordinated to the metal hydride Ru-H resulted in the quick formation of Ru-H-CO$_2$ species, corresponding to the peaks from 1240 to 1270 cm^{-1} [23,57]. The H-bound formate intermediate subsequently by rotational rearrangement to produce an O-bound formate intermediate (Ru-COOH) [56]. The peaks at 1359, 1539, 1555, 1572, 1683, 1697, 1732 and 1748 cm^{-1} corresponding to Ru-COOH also increased as time went on, demonstrating that Ru-COOH was a crucial intermediate for the photo-reduced conversion of CO$_2$ to formic acid [58–61]. Moreover, the peaks at 1455, 1607, 1772, 1794 and 1828 cm^{-1} were ascribed to formate ion (HCOO⁻) [23,62].

Then, the relative Gibbs free energy (ΔG) diagram (Fig. 5e) along with detailed conversion pathway (Fig. 5d) was constructed by using DFT calculations based on the information obtained from *in situ* ATR-IR. According to the results of XAFS measurements, one of the carbonyl ligands (CO) in Ru-CTF was substituted by a H$_2$O molecule in this work. Thus, in the process of CO$_2$RR, the metal hydride [Ru-H]$^{-2}$ intermediate was more likely to form through the substitution of H$_2$O site ($\Delta G = -0.22$ eV) rather than the substitution of chlorine (Cl) ($\Delta G = +3.22$ eV) or carbonyl ligands (CO) ($\Delta G = +1.81$ eV) in Ru-CTF (Fig. S29). This result indicated that the water-substituted Ru unit was more favorable for the photocatalytic CO$_2$RR than the dicarbonyl precursors. In the process of CO$_2$RR, the exited CTF support could be oxidatively quenched by Ru-N$_2$ unit to drive the [Ru-H$_2$O]^0 to generate [Ru-H$_2$O]$^{-2}$ at first. Followed a [H$_2$O] loss and reacts with H⁺ and e⁻ to generate metal hydride [Ru-H]$^{-2}$. Here, TEOA was the proton and electron sources for the metal hydride generation [56]. Then metal hydride can react with CO$_2$ to generate a [Ru-H-CO$_2$]$^{-2}$ adduct [44,56]. The formation of the [Ru-H-CO$_2$]$^{-2}$(TS) intermediate was found to be the rate-limiting step for CO$_2$ to HCOO⁻. The transiently formed H-bound formate intermediate [Ru-H-CO$_2$]$^{-2}$ underwent a rotational rearrangement to obtain the O-bound highly stable intermediate [Ru-COOH]$^{-2}$ ($\Delta G = -0.28$ eV). Finally, the HCOO⁻ could be released from the catalyst to recover the initial state. The exited CTF support could be reduced to original state by TEOA, completing the photocatalytic cycle. All the intermediate steps as revealed from the relative Gibbs free energy calculations exhibited high thermodynamic feasibility. The results of *in situ* ATR-IR and DFT calculations demonstrate that the single-site Ru-N$_2$ is the active center simultaneously for CO$_2$ activation and the H$_2$O-substituted Ru unit is more favorable to form the key intermediate metal hydride to react with
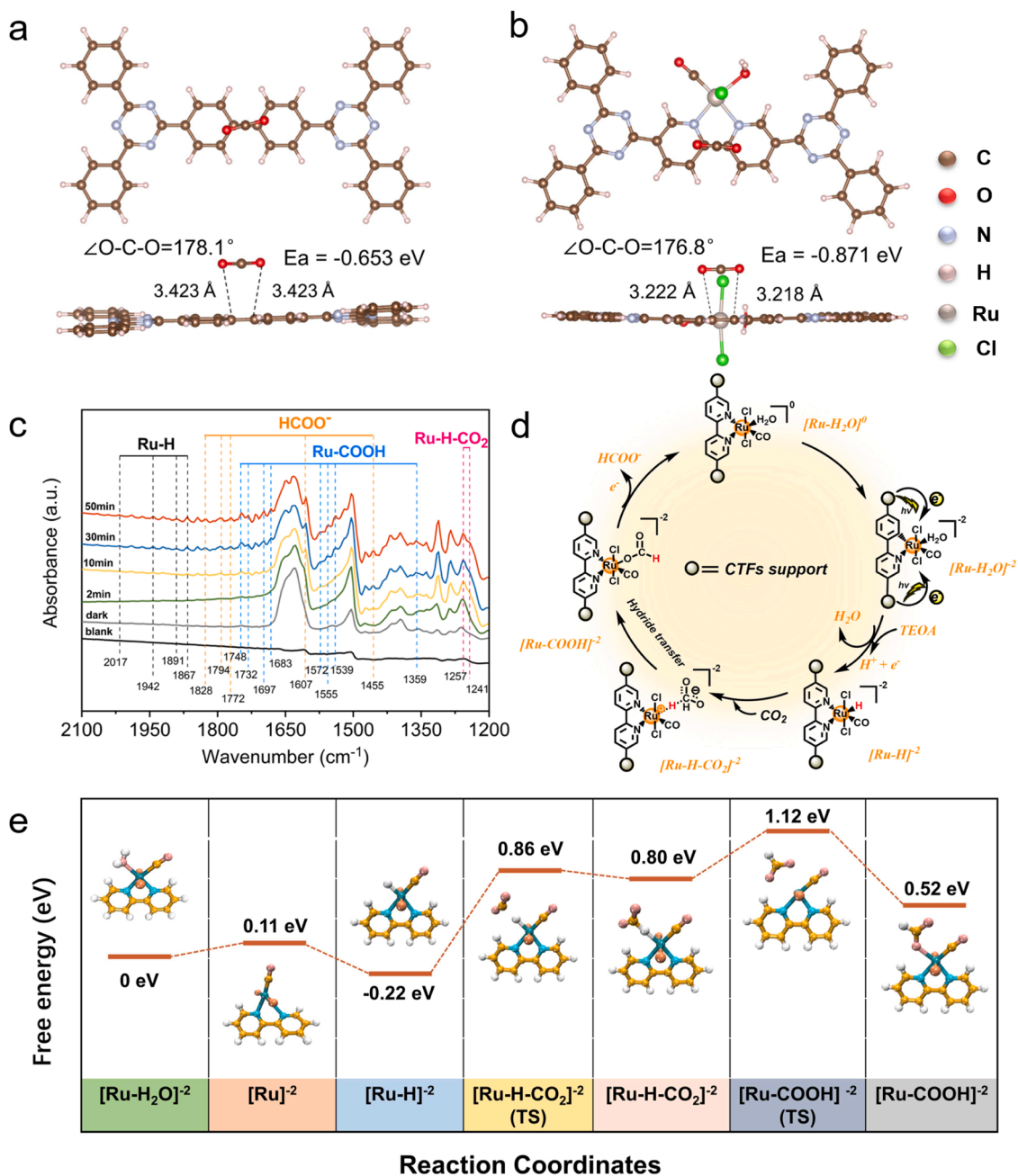
Fig. 5. Adsorption energy of CO_2 on (a) dcbph-CTF and (b) Ru-CTF surface. (c) *In situ* attenuated total reflection-infrared (ATR-IR) of Ru-CTF samples in specific analysis. (d) Proposed catalytic mechanism with the molecular unit of Ru-N_2 for photocatalytic CO_2 reduction to HCOOH. (e) Gibbs free energy pathway for the formation of formate from CO_2.

CO_2 with a much lower free energy barrier than that of dicarbonyl precursors, which may realize high catalytic activity of Ru-CTF for CO_2RR.

4. Conclusions

In summary, we present an efficient Ru-CTF photocatalyst for the conversion of CO_2 to formate by knitting molecular catalysts into highly conjugated and photoresponsive CTFs with an *in situ* covalent-bonding strategy. The strong chemical knitting of molecular catalyst into highly conjugated CTFs affords the atomically dispersed Ru-N_2 sites, and the resulting single-site Ru-CTF can serve as efficient platform to bridge the gap between homogeneous catalysts and heterogeneous catalysts, thereby significantly improving photocatalytic activities. Remarkably,

the efficient electron transfer from triazine units to Ru-N_2 catalytic centers allowed excellent selectivity and remarkable formate production rate under visible light. In addition, systematic DFT calculations were used to detailedly assess the electronic structures and possible reaction pathways. Our findings provide important insights into rational design and synthesis of π-conjugated CTF-based semiconducting polymers from the molecular level for photocatalytic CO_2 conversion. Furthermore, we believe that the *in situ* knitting strategy of single-site CTFs hold enormous potential for energy-related photocatalysis.

CRediT authorship contribution statement

Lu Wang and **Lin Wang** contributed equally to this work. **Lu Wang:** Conceptualization, Methodology, Writing – original draft, Writing –

review & editing, Visualization, Investigation. **Lin Wang:** Writing – review & editing, Investigation, Validation, Supervision, Project administration, Funding acquisition. **Saifei Yuan:** Software. **Liping Song:** Software. **Hao Ren:** Software, Formal analysis. **Yuankang Xu:** Validation. **Manman He:** Formal analysis. **Yuheng Zhang:** Formal analysis. **Hang Wang:** Validation, Formal analysis. **Yichao Huang:** Validation, Software, Formal analysis. **Tong Wei:** Supervision, Project administration, Funding acquisition, Resources. **Jiangwei Zhang:** Software, Formal analysis, Visualization, Data curation. **Yuichiro Himeda:** Supervision, Validation. **Zhuangjun Fan:** Investigation, Validation, Supervision, Project administration, Funding acquisition.

Declaration of Competing Interest

The authors declare that they have no known competing financial interests or personal relationships that could have appeared to influence the work reported in this paper.

Data availability

Supplementary data to this article can be found online.

Appendix A. Supporting information

Supplementary data associated with this article can be found in the online version at doi:10.1016/j.apcatb.2022.122097.

References

[1] Z. Deng, S. Hu, J. Ji, S. Wu, H. Xie, M. Xing, J. Zhang, Deep insight of the influence of Cu valence states in co-catalyst on CO_2 photoreduction, Appl. Catal. B 316 (2022), 121621.

[2] J. Wang, Y. Yu, J. Cui, X. Li, Y. Zhang, C. Wang, X. Yu, J. Ye, Defective g-C_3N_4/ covalent organic framework van der Waals heterojunction toward highly efficient S-scheme CO_2 photoreduction, Appl. Catal. B 301 (2022), 120814.

[3] A.C. Ghosh, A. Legrand, R. Rajapaksha, G.A. Craig, C. Sassoye, G. Balázs, D. Farrusseng, S. Furukawa, J. Canivet, F.M. Wisser, Rhodium-based metal–organic polyhedra assemblies for selective CO_2 photoreduction, J. Am. Chem. Soc. 144 (2022) 3626–3636.

[4] J.-S. Qin, S. Yuan, L. Zhang, B. Li, D.-Y. Du, N. Huang, W. Guan, H.F. Drake, J. Pang, Y.-Q. Lan, A. Alsalme, H.-C. Zhou, Creating well-defined hexabenzocoronene in zirconium metal–organic framework by postsynthetic annulation, J. Am. Chem. Soc. 141 (2019) 2054–2060.

[5] H.-Q. Xu, J. Hu, D. Wang, Z. Li, Q. Zhang, Y. Luo, S.-H. Yu, H.-L. Jiang, Visible-light photoreduction of CO_2 in a metal–organic framework: boosting electron–hole separation via electron trap states, J. Am. Chem. Soc. 137 (2015) 13440–13443.

[6] N. Li, J. Liu, J.-J. Liu, L.-Z. Dong, Z.-F. Xin, Y.-L. Teng, Y.-Q. Lan, Adenine components in biomimetic metal–organic frameworks for efficient CO_2 photoconversion, Angew. Chem. Int Ed. 58 (2019) 5226–5231.

[7] M. Elcheikh Mahmoud, H. Audi, A. Assoud, T.H. Ghaddar, M. Hmadeh, Metal–organic framework photocatalyst incorporating bis(4′-(4-carboxyphenyl)-terpyridine)ruthenium(II) for visible-light-driven carbon dioxide reduction, J. Am. Chem. Soc. 141 (2019) 7115–7121.

[8] T.-C. Zhuo, Y. Song, G.-L. Zhuang, L.-P. Chang, S. Yao, W. Zhang, Y. Wang, P. Wang, W. Lin, T.-B. Lu, Z.-M. Zhang, H-bond-mediated selectivity control of formate versus CO during CO_2 photoreduction with two cooperative Cu/X sites, J. Am. Chem. Soc. 143 (2021) 6114–6122.

[9] J.-Y. Zeng, X.-S. Wang, B.-R. Xie, Q.-R. Li, X.-Z. Zhang, Large π-conjugated metal–organic frameworks for infrared-light-driven CO_2 reduction, J. Am. Chem. Soc. 144 (2022) 1218–1231.

[10] F.M. Wisser, M. Duguet, Q. Perrinet, A.C. Ghosh, M. Alves-Favaro, Y. Mohr, C. Lorentz, E.A. Quadrelli, R. Palkovits, D. Farrusseng, C. Mellot-Draznieks, V. de Waele, J. Canivet, Molecular porous photosystems tailored for long-term photocatalytic CO_2 reduction, Angew. Chem. Int Ed. 59 (2020) 5116–5122.

[11] J.-J. Liu, N. Li, J.-W. Sun, J. Liu, L.-Z. Dong, S.-J. Yao, L. Zhang, Z.-F. Xin, J.-W. Shi, J.-X. Wang, S.-L. Li, Y.-Q. Lan, Ferrocene-functionalized polyoxo-titanium cluster for CO_2 photoreduction, ACS Catal. 11 (2021) 4510–4519.

[12] N. Li, J. Liu, J.-J. Liu, L.-Z. Dong, S.-L. Li, B.-X. Dong, Y.-H. Kan, Y.-Q. Lan, Self-assembly of a phosphate-centered polyoxo-titanium cluster: discovery of the heteroatom Keggin family, Angew. Chem. Int Ed. 58 (2019) 17260–17264.

[13] H. Zhang, Y. Li, J. Wang, N. Wu, H. Sheng, C. Chen, J. Zhao, An unpreced hydride transfer pathway for selective photocatalytic reduction of CO_2 to formic acid on TiO_2, Appl. Catal. B 284 (2021), 119692.

[14] Y.-N. Gong, W. Zhong, Y. Li, Y. Qiu, L. Zheng, J. Jiang, H.-L. Jiang, Regulating photocatalysis by spin-state manipulation of cobalt in covalent organic frameworks, J. Am. Chem. Soc. 142 (2020) 16723–16731.

[15] Z. Zhao, D. Zheng, M. Guo, J. Yu, S. Zhang, Z. Zhang, Y. Chen, Engineering Olefin-linked covalent organic frameworks for photoenzymatic reduction of CO_2, Angew. Chem. Int Ed. 61 (2022), e202200261.

[16] S. Enthaler, J. von Langermann, T. Schmidt, Carbon dioxide and formic acid—the couple for environmental-friendly hydrogen storage? Energy Environ. Sci. 3 (2010) 1207–1217.

[17] M. Liu, Y. Xu, Y. Meng, L. Wang, H. Wang, Y. Huang, N. Onishi, L. Wang, Z. Fan, Y. Himeda, Heterogeneous catalysis for carbon dioxide mediated hydrogen storage technology based on formic acid, Adv. Energy Mater. 12 (2022), 2200817.

[18] R. Kuriki, K. Sekizawa, O. Ishitani, K. Maeda, Visible-light-driven CO_2 reduction with carbon nitride: enhancing the activity of ruthenium catalysts, Angew. Chem. Int Ed. 54 (2015) 2406–2409.

[19] S. Sato, T. Morikawa, S. Saeki, T. Kajino, T. Motohiro, Visible-light-induced selective CO_2 reduction utilizing a ruthenium complex electrocatalyst linked to a p-type nitrogen-doped Ta_2O_5 semiconductor, Angew. Chem. Int Ed. 49 (2010) 5101–5105.

[20] K. Sekizawa, S. Sato, T. Arai, T. Morikawa, Solar-driven photocatalytic CO_2 reduction in water utilizing a ruthenium complex catalyst on p-type Fe_2O_3 with a multiheterojunction, ACS Catal. 8 (2018) 1405–1416.

[21] R. Kuriki, H. Matsunaga, T. Nakashima, K. Wada, A. Yamakata, O. Ishitani, K. Maeda, Nature-inspired, highly durable CO_2 reduction system consisting of a binuclear Ruthenium(II) complex and an organic semiconductor using visible light, J. Am. Chem. Soc. 138 (2016) 5159–5170.

[22] R. Kuriki, M. Yamamoto, K. Higuchi, Y. Yamamoto, M. Akatsuka, D. Lu, S. Yagi, T. Yoshida, O. Ishitani, K. Maeda, Robust binding between carbon nitride nanosheets and a binuclear ruthenium(ii) complex enabling durable, selective CO_2 reduction under visible light in aqueous solution, Angew. Chem. Int Ed. 56 (2017) 4867–4871.

[23] M. Kou, W. Liu, Y. Wang, J. Huang, Y. Chen, Y. Zhou, Y. Chen, M. Ma, K. Lei, H. Xie, P.K. Wong, L. Ye, Photocatalytic CO_2 conversion over single-atom MoN_2 sites of covalent organic framework, Appl. Catal. B 291 (2021), 120146.

[24] S. Yang, W. Hu, X. Zhang, P. He, B. Pattengale, C. Liu, M. Cendejas, I. Hermans, X. Zhang, J. Zhang, J. Huang, 2D covalent organic frameworks as intrinsic photocatalysts for visible light-driven CO_2 reduction, J. Am. Chem. Soc. 140 (2018) 14614–14618.

[25] Y. Fu, X. Zhu, L. Huang, X. Zhang, F. Zhang, W. Zhu, Azine-based covalent organic frameworks as metal-free visible light photocatalysts for CO_2 reduction with H_2O, Appl. Catal. B 239 (2018) 46–51.

[26] M. Lu, M. Zhang, J. Liu, T.-Y. Yu, J.-N. Chang, L.-J. Shang, S.-L. Li, Y.-Q. Lan, Confining and highly dispersing single polyoxometalate clusters in covalent organic frameworks by covalent linkages for CO_2 photoreduction, J. Am. Chem. Soc. 144 (2022) 1861–1871.

[27] Z.-H. Yan, M.-H. Du, J. Liu, S. Jin, C. Wang, G.-L. Zhuang, X.-J. Kong, L.-S. Long, L.-S. Zheng, Photo-generated dinuclear {Eu(II)}$_2$ active sites for selective CO_2 reduction in a photosensitizing metal-organic framework, Nat. Commun. 9 (2018) 3353.

[28] X. Feng, Y. Pi, Y. Song, C. Brzezinski, Z. Xu, Z. Li, W. Lin, Metal–organic frameworks significantly enhance photocatalytic hydrogen evolution and CO_2 reduction with earth-abundant copper photosensitizers, J. Am. Chem. Soc. 142 (2020) 690–695.

[29] S. Wang, X. Hai, X. Ding, S. Jin, Y. Xiang, P. Wang, B. Jiang, F. Ichihara, M. Oshikiri, X. Meng, Y. Li, W. Matsuda, J. Ma, S. Seki, X. Wang, H. Huang, Y. Wada, H. Chen, J. Ye, Intermolecular cascaded π-conjugation channels for electron delivery powering CO_2 photoreduction, Nat. Commun. 11 (2020) 1149.

[30] S. Barman, A. Singh, F.A. Rahimi, T.K. Maji, Metal-free catalysis: a redox-active donor–acceptor conjugated microporous polymer for selective visible-light-driven CO_2 reduction to CH_4, J. Am. Chem. Soc. 143 (2021) 16284–16292.

[31] G. Huang, Q. Niu, J. Zhang, H. Huang, Q. Chen, J. Bi, L. Wu, Platinum single-atoms anchored covalent triazine framework for efficient photoreduction of CO_2 to CH_4, Chem. Eng. J. 427 (2022), 131018.

[32] P. Kuhn, M. Antonietti, A. Thomas, Porous, covalent triazine-based frameworks prepared by ionothermal synthesis, Angew. Chem. Int Ed. 47 (2008) 3450–3453.

[33] Y. Hu, W. Huang, H. Wang, Q. He, Y. Zhou, P. Yang, Y. Li, Y. Li, Metal-free photocatalytic hydrogenation using covalent triazine polymers, Angew. Chem. Int Ed. 59 (2020) 14378–14382.

[34] C. Wang, H. Zhang, W. Luo, T. Sun, Y. Xu, Ultrathin crystalline covalent-triazine-framework nanosheets with electron donor groups for synergistically enhanced photocatalytic water splitting, Angew. Chem. Int. Ed. 60 (2021) 25381–25390.

[35] X. Zhu, C. Tian, G.M. Veith, C.W. Abney, J. Dehaudt, S. Dai, In situ doping strategy for the preparation of conjugated triazine frameworks displaying efficient CO_2 capture performance, J. Am. Chem. Soc. 138 (2016) 11497–11500.

[36] M. Mahato, S. Nam, R. Tabassian, S. Oh, V.H. Nguyen, I.-K. Oh, Electronically conjugated multifunctional covalent Triazine framework for unprecedented CO_2

selectivity and high-power flexible supercapacitor, Adv. Funct. Mater. 32 (2022), 2107442.

[37] W. Huang, Q. He, Y. Hu, Y. Li, Molecular Heterostructures of covalent triazine frameworks for enhanced photocatalytic hydrogen production, Angew. Chem. Int Ed. 58 (2019) 8676–8680.

[38] L. Zeng, J.-W. Chen, L. Zhong, W. Zhen, Y.Y. Tay, S. Li, Y.-G. Wang, L. Huang, C. Xue, Synergistic effect of Ru-N$_4$ sites and Cu-N$_3$ sites in carbon nitride for highly selective photocatalytic reduction of CO$_2$ to methane, Appl. Catal. B 307 (2022), 121154.

[39] X. Xiong, C. Mao, Z. Yang, Q. Zhang, G.I.N. Waterhouse, L. Gu, T. Zhang, Photocatalytic CO$_2$ reduction to CO over Ni single atoms supported on defect-rich Zirconia, Adv. Energy Mater. 10 (2020), 2002928.

[40] J.-X. Jiang, C. Wang, A. Laybourn, T. Hasell, R. Clowes, Y.Z. Khimyak, J. Xiao, S. J. Higgins, D.J. Adams, A.I. Cooper, Metal–organic conjugated microporous polymers, Angew. Chem. Int. Ed. 50 (2011) 1072–1075.

[41] D. Preti, S. Squarcialupi, G. Fachinetti, Production of HCOOH/NEt$_3$ adducts by CO$_2$/H$_2$ incorporation into neat NEt$_3$, Angew. Chem. Int Ed. 49 (2010) 2581–2584.

[42] T. Schaub, R.A. Paciello, A process for the synthesis of formic acid by CO2 hydrogenation: thermodynamic aspects and the role of CO, Angew. Chem. Int. Ed. 50 (2011) 7278–7282.

[43] M.K. Saini, H.S. Korawat, S.K. Verma, A.K. Basak, Pyridinium triflate catalyzed intramolecular alkyne-carbonyl metathesis reaction of O-propargylated 2-hydroxyarylaldehydes, Tetrahedron Lett. 61 (2020), 152657.

[44] B. Shan, S. Vanka, T.-T. Li, L. Troian-Gautier, M.K. Brennaman, Z. Mi, T.J. Meyer, Binary molecular-semiconductor p–n junctions for photoelectrocatalytic CO$_2$ reduction, Nat. Energy 4 (2019) 290–299.

[45] P.A. Anderson, G.B. Deacon, K.H. Haarmann, F.R. Keene, T.J. Meyer, D.A. Reitsma, B.W. Skelton, G.F. Strouse, N.C. Thomas, Designed synthesis of mononuclear tris (heteroleptic) ruthenium complexes containing bidentate polypyridyl ligands, Inorg. Chem. 34 (1995) 6145–6157.

[46] Z.-A. Lan, Y. Fang, Y. Zhang, X. Wang, Photocatalytic oxygen evolution from functional triazine-based polymers with tunable band structures, Angew. Chem. Int. Ed. 57 (2018) 470–474.

[47] L. Spiccia, G.B. Deacon, C.M. Kepert, Synthetic routes to homoleptic and heteroleptic ruthenium(II) complexes incorporating bidentate imine ligands, Coord. Chem. Rev. 248 (2004) 1329–1341.

[48] C. Agnès, J.-C. Arnault, F. Omnès, B. Jousselme, M. Billon, G. Bidan, P. Mailley, XPS study of ruthenium tris-bipyridine electrografted from diazonium salt derivative on microcrystalline boron doped diamond, Phys. Chem. Chem. Phys. 11 (2009) 11647–11654.

[49] L. Chen, L. Wang, Y. Wan, Y. Zhang, Z. Qi, X. Wu, H. Xu, Acetylene and diacetylene functionalized covalent triazine frameworks as metal-free photocatalysts for hydrogen peroxide production: a new two-electron water oxidation pathway, Adv. Mater. 32 (2020), 1904433.

[50] Z. Yang, H. Chen, S. Wang, W. Guo, T. Wang, X. Suo, D.-e Jiang, X. Zhu, I. Popovs, S. Dai, Transformation strategy for highly crystalline covalent triazine frameworks: from staggered AB to eclipsed AA stacking, J. Am. Chem. Soc. 142 (2020) 6856–6860.

[51] G.H. Gunasekar, J. Shin, K.-D. Jung, K. Park, S. Yoon, Design strategy toward recyclable and highly efficient heterogeneous catalysts for the hydrogenation of CO$_2$ to formate, ACS Catal. 8 (2018) 4346–4353.

[52] D. Sun, Y. Gao, J. Fu, X. Zeng, Z. Chen, Z. Li, Construction of a supported Ru complex on bifunctional MOF-253 for photocatalytic CO$_2$ reduction under visible light, Chem. Commun. 51 (2015) 2645–2648.

[53] C. Gao, J. Wang, H. Xu, Y. Xiong, Coordination chemistry in the design of heterogeneous photocatalysts, Chem. Soc. Rev. 46 (2017) 2799–2823.

[54] R.A. Belisle, W.H. Nguyen, A.R. Bowring, P. Calado, X. Li, S.J.C. Irvine, M. D. McGehee, P.R.F. Barnes, B.C. O'Regan, Interpretation of inverted photocurrent transients in organic lead halide perovskite solar cells: proof of the field screening by mobile ions and determination of the space charge layer widths, Energy Environ. Sci. 10 (2017) 192–204.

[55] S. Luukkanen, M. Haukka, E. Eskelinen, T.A. Pakkanen, V. Lehtovuori, J. Kallioinen, P. Myllyperkiö, J. Korppi-Tommola, Photochemical reactivity of halogen-containing ruthenium–dcbpy (dcbpy = 4,4′-dicarboxylic acid-2,2′-bipyridine) compounds, trans(Br)-[Ru(dcbpy)(CO)$_2$Br$_2$] and trans(I)-[Ru(dcbpy) (CO)$_2$I$_2$], Phys. Chem. Chem. Phys. 3 (2001) 1992–1998.

[56] R.N. Sampaio, D.C. Grills, D.E. Polyansky, D.J. Szalda, E. Fujita, Unexpected roles of triethanolamine in the photochemical reduction of CO$_2$ to formate by Ruthenium complexes, J. Am. Chem. Soc. 142 (2020) 2413–2428.

[57] D. Wang, R. Huang, W. Liu, D. Sun, Z. Li, Fe-based MOFs for photocatalytic CO$_2$ reduction: role of coordination unsaturated sites and dual excitation pathways, ACS Catal. 4 (2014) 4254–4260.

[58] S. Karmakar, S. Barman, F.A. Rahimi, T.K. Maji, Covalent grafting of molecular photosensitizer and catalyst on MOF-808: effect of pore confinement toward visible light-driven CO$_2$ reduction in water, Energy Environ. Sci. 14 (2021) 2429–2440.

[59] J. Li, B. Huang, Q. Guo, S. Guo, Z. Peng, J. Liu, Q. Tian, Y. Yang, Q. Xu, Z. Liu, B. Liu, Van der Waals heterojunction for selective visible-light-driven photocatalytic CO$_2$ reduction, Appl. Catal. B 284 (2021), 119733.

[60] C. Yang, Q. Tan, Q. Li, J. Zhou, J. Fan, B. Li, J. Sun, K. Lv, 2D/2D Ti$_3$C$_2$ MXene/g-C$_3$N$_4$ nanosheets heterojunction for high efficient CO$_2$ reduction photocatalyst: dual effects of urea, Appl. Catal. B 268 (2020), 118738.

[61] H. Pang, X. Meng, P. Li, K. Chang, W. Zhou, X. Wang, X. Zhang, W. Jevasuwan, N. Fukata, D. Wang, J. Ye, Cation vacancy-initiated CO$_2$ photoreduction over ZnS for efficient formate production, ACS Energy Lett. 4 (2019) 1387–1393.

[62] Y. Li, B. Li, D. Zhang, L. Cheng, Q. Xiang, Crystalline carbon nitride supported copper single atoms for photocatalytic CO$_2$ reduction with nearly 100% CO selectivity, ACS Nano 14 (2020) 10552–10561.